nature chemistry

SUPPLEMENTARY INFORMATION

https://doi.org/10.1038/s41557-019-0263-4

In the format provided by the authors and unedited.

Imaging defects and their evolution in a metal–organic framework at sub-unit-cell resolution

Lingmei Liu[1,9], Zhijie Chen[2,9], Jianjian Wang[1,3,9], Daliang Zhang[4]*, Yihan Zhu[5], Sanliang Ling[6], Kuo-Wei Huang[7], Youssef Belmabkhout[2], Karim Adil[2], Yuxin Zhang[3], Ben Slater[8]*, Mohamed Eddaoudi[2]* and Yu Han[1,7]*

[1]King Abdullah University of Science and Technology (KAUST), Physical Sciences and Engineering Division, Advanced Membranes and Porous Materials (AMPM) Center, Thuwal, Saudi Arabia. [2]KAUST, Physical Sciences and Engineering Division, AMPM Center, Functional Materials Design, Discovery and Development Research Group (FMD3), Thuwal, Saudi Arabia. [3]Multi-scale Porous Materials Center, Institute of Advanced Interdisciplinary Studies, Chongqing University, Chongqing, China. [4]KAUST, Core Labs, Thuwal, Saudi Arabia. [5]Department of Chemical Engineering, Zhejiang University of Technology, Hangzhou, China. [6]Advanced Materials Research Group, Faculty of Engineering, University of Nottingham, University Park, Nottingham, UK. [7]KAUST, KAUST Catalysis Center (KCC), Thuwal, Saudi Arabia. [8]Department of Chemistry, University College London, London, UK. [9]These authors contributed equally: Lingmei Liu, Zhijie Chen, Jianjian Wang. *e-mail: daliang.zhang@kaust.edu.sa; b.slater@ucl.ac.uk; mohamed.eddaoudi@kaust.edu.sa; yu.han@kaust.edu.sa

Supplementary Materials

Imaging defects and their evolution in a metal–organic framework at sub-unit-cell resolution

Lingmei Liu,[1,⊥] Zhijie Chen,[2,⊥] Jianjian Wang,[1,7,⊥] Daliang Zhang,[3,*] Yihan Zhu,[4] Sanliang Ling,[5] Kuo-wei Huang,[6] Youssef Belmabkhout,[2] Karim Adil,[2] Yuxin Zhang,[7] Ben Slater,[8,*] Mohamed Eddaoudi,[2,*] Yu Han[1,6,*]

[1] King Abdullah University of Science and Technology (KAUST), Physical Sciences and Engineering Division, Advanced Membranes and Porous Materials (AMPM) Center, Thuwal 23955-6900, Saudi Arabia
[2] KAUST, Physical Sciences and Engineering Division, AMPM Center, Functional Materials Design, Discovery and Development Research Group (FMD[3]), Thuwal 23955-6900, Saudi Arabia
[3] KAUST, Core Labs, Thuwal, 23955-6900, Saudi Arabia
[4] Department of Chemical Engineering, Zhejiang University of Technology, Hangzhou 310014, P.R. China
[5] Advanced Materials Research Group, Faculty of Engineering, University of Nottingham, University Park, Nottingham NG7 2RD, United Kingdom
[6] KAUST, KAUST Catalysis Center (KCC), Thuwal 23955-6900, Saudi Arabia
[7] Multi-scale Porous Materials Center, Institute of Advanced Interdisciplinary Studies & College of Materials Science and Engineering, Chongqing University, Chongqing 400044, P. R. China
[8] Department of Chemistry, University College London, 20 Gordon Street, London WC1H 0AJ, United Kingdom

[⊥] These authors contributed equally to this work.

*Corresponding author. Email: daliang.zhang@kaust.edu.sa; b.slater@ucl.ac.uk; mohamed.eddaoudi@kaust.edu.sa; yu.han@kaust.edu.sa

This PDF file includes:

Separate Supporting files:

Atomic coordinates of optimised structures are listed in separate CIF files.

Methods

Synthesis of materials

Synthesis of UiO-66-D

Terephthalic acid (230 mg, 1.4 mmol), $ZrOCl_2 \cdot 8H_2O$ (460 mg, 1.4 mmol), formic acid (2.65 mL, 70 mmol), and DMF (23 mL) were ultrasonically mixed in a 34 mL vial (PYREX® Culture Tubes, Reusable, Borosilicate Glass, With Screw Cap, Corning®). The mixture was then sealed and heated to 120 °C for 24 h and cooled to room temperature. The obtained white powders were collected by centrifugation (6000 rpm for 30min), and then washed 6 times over 3 days with 40 mL of anhydrous DMF and then sequentially immersed in 40 mL of methanol for 3 days, during which time the methanol was replaced twice per day. The solids were then dried at 120 °C under vacuum for 24 h for characterizations.

Two more UiO-66 samples were synthesized by following the same procedure described above but varying the crystallization time to 1 h, and 72 h (3 days), respectively.

The UiO-66 samples using 175 molar equivalents of formic acid relative to BDC were synthesized by following the previously reported protocols [25] with varied crystallization time.

Synthesis of UiO-66-P

Terephthalic acid (133 mg, 0.80 mmol), $ZrCl_4$ (203 mg, 0.87 mmol), acetic acid (24 mL), and DMF (200 mL) were mixed in a 1000 mL bottle (Kimble® 14395-1000 KIMAX® 1000mL Round Glass Media Bottle with Blue PP GL45 Screw Cap, Graduated). The bottle was sealed and then heated to 120 °C for 48 h and cooled to room temperature. The obtained white powders were collected by centrifugation (5500 rpm for 5min), and then washed 6 times over 3 days with 30 mL of anhydrous DMF and then sequentially immersed in 50 mL of methanol for 3 days, during which time the methanol was replaced twice per day. The solid was then dried at 120 °C under vacuum for 24 h for characterizations.

Healing of missing linker defects in UiO-66-D

A post-synthesis ligand-exchange method was used to heal the missing linker defects. Specifically, 100 mg of defective sample (UiO-66-D(3d)) was dispersed in 8 mL of water and DMF (9:1, V/V); 80 mg of terephthalate acid was added into the solution; the mixture was ultrasonicated for 10 min, and then placed into a preheated (80 °C) oven for 1 d to facilitate ligand exchange (replacing formates with terephthalates). After cooling to the room temperature, the solid product was collected by centrifugation (8000 rpm for 3 min), thoroughly washed with DMF/methanol for several times, and dried at 120 °C overnight under vacuum. This process was repeated to achieve a higher degree of healing of the missing linker defects.

Powder X-ray diffraction

Powder X-ray Diffraction Patterns were recorded on using a Bruker D8 Advance instrument with Cu Kα radiation (λ = 0.1542 nm) operated at 40 kV and 40 mA with a scanning speed at 0.5 degree per minute.

N_2 gas adsorption measurements

N_2 gas adsorption isotherms were collected on a Micromeritics 3Flex Surface Characterization Analyzer system at relative pressures up to 1 atm. The cryogenic temperature was controlled using liquid nitrogen bath at 77 K. The apparent surface areas were derived by applying the Brunauer-Emmett-Teller (BET) model. The pore size distribution profiles were determined based on the pillared clay model using a nonlocal density functional theory (NLDFT) method.

Determination of the formate content in UiO-66 samples

High-performance liquid chromatography (HPLC) was used to measure the concentration of formic acid in the digested solution of UiO-66, so as to determine the content of formate in the solids, assuming that all the formates are extracted into the solution by the digestion. Typically, the UiO-66 sample (100 mg) was digested in 1mL of HF aqueous solution (3.5 wt%); after centrifugation, the upper clear solution was analyzed by an HPLC apparatus (Agilent 1260 Series) equipped with an Aminex HPX-87H ion-exclusion column operated at 50 °C. The eluent used was 0.5 mM H_2SO_4 solution at a flow rate of 0.5 mL/min. Formic acid in the digested solution was detected with a refractive index detector (RID), and its content was determined based on the external standard method.

Catalytic isomerization reaction of glucose to fructose

The reactions were performed in a Parr stainless steel autoclave (25 mL). Typically, 80 mg of glucose, 14 mg of catalyst (vacuum-dried at 120 °C prior to use), and 10 mL of isopropanol solvent were mixed in the reactor with a magnetic stirring at 200 rpm. Nitrogen was used to purge the reactor before the reaction. After the reaction at 90 °C for 12 h, the reactor was cooled down to room temperature. The solid catalyst was removed by centrifugation, and the upper clear solution was taken for HPLC analysis without dilution. The analysis of glucose conversion and fructose yield was carried out on HPLC apparatus (Agilent 1260 Series) equipped with an Aminex HPX-87H ion-exclusion column operated at 50 °C. The eluent used was 0.5 mM H_2SO_4 solution (0.5 mL/min). Glucose and fructose were detected with a refractive index detector (RID), and quantified based on the external standard method.

TEM imaging and simulation

TEM experiments were performed on a Cs-corrected FEI Titan Cube transmission electron microscope at an acceleration voltage of 300 kV. Spherical aberration (Cs) values were corrected to be in a range of ±5 μm. Specimen searching, zone axis alignment, and pre-focusing were conducted with a dose rate of 0.01 ~ 0.03 e/Å^2/s. HRTEM images were acquired at a magnification of 55 k by a Gatan K2 direct-detection camera in the electron-counting mode with the dose fractionation function. Electron diffraction patterns were collected using a Gatan Ultra-scan CCD camera. Crystal zone axis alignment and image processing were performed by a self-developed software package [33]. Projected potentials were simulated by QSTEM

software [Supp. Ref. 1] with a point spread function width of 2 Å.

Contrast Transfer Function (CTF) correction of HRTEM images

In order to perform CTF correction, we need to know the exact defocus astigmatism values of the acquired HRTEM images. In our previous work, we reported a method to determine these values. Specifically, after acquiring each HRTEM image, we purposely amorphize the imaged area by electron beam and then take an image for the resulting amorphous region to determine the defocus and astigmatism values by analyzing the thon rings. In this study, we realized that the specimen usually shrinks to certain extent when amorphized, possibly because of the small particle size, which has no influence on the determination of astigmatism but could result in small deviation in the determined defocus from the actual value. In order to get more accurate defocus, we calculate a series of CTF-corrected images by using different defocus values (± 100 nm around the determined defocus with 1 nm interval); then, we apply lattice averaging to each calculated image to enhance the signal-to-noise ratio; finally, we compare the contrast of Zr_6O_8 cluster between these averaged images and determine the defocus to be the one that gives the best matching with the simulated potential/structural model (we assume that the structural integrity of metal clusters is always retained regardless of the connectivity). For clarification, an example of how we determine the defocus is provided in Supplementary Fig. 16.

Reconstruction by electron crystallography

The missing linker defect was three dimensionally reconstructed by electron crystallography from three HRTEM images acquired along the [001], [100] and [110] zone axis, respectively. Specifically, reflections with amplitudes larger than s threshold value (4% of the amplitude of the strongest reflection in a given incidence) were extracted from HRTEM images using software CRISP [Supp. Ref. 2] (Supplementary Table 3). Reflections from three zone axes were normalized and merged into one combined dataset with adjusted phase origin according to common reflections (Supplementary Table 4). Electron potential maps were obtained by Fourier synthesis using software Vesta [Supp. Ref. 3].

Computational Details

All density functional theory (DFT) calculations have been performed using the CP2K code, which uses a mixed Gaussian/plane-wave basis set. [Supp. Ref. 4-5] We employed double-ζ polarization quality Gaussian basis sets [Supp. Ref. 6] and a 600 Ry plane-wave cutoff for the auxiliary grid, in conjunction with the Goedecker-Teter-Hutter pseudopotentials [Supp. Ref. 7-8]. A convergence threshold of 1.0×10^{-8} Ha was used for the self-consistent field cycle; structural optimizations were considered as converged when the maximum force on atoms fell below 1.0×10^{-4} Ha $Bohr^{-1}$. All calculations were performed in the Γ-point approximation for sufficiently large cells, e.g. the total number of atoms in the fcu, bcu, reo and scu cells are 456, 392, 294 and 262, respectively. All DFT calculations, including single point energies and geometry/cell optimizations, were performed using the PBE functional [Supp. Ref. 9], with Grimme's D3 van der Waals correction (PBE+D3) [Supp. Ref. 10]. This method was shown to give very good agreement with experimental structural data on several MOFs which we studied previously [Supp. Ref. 11-12]. Cell parameters of DFT calculations are given as Supplementary Table 5.

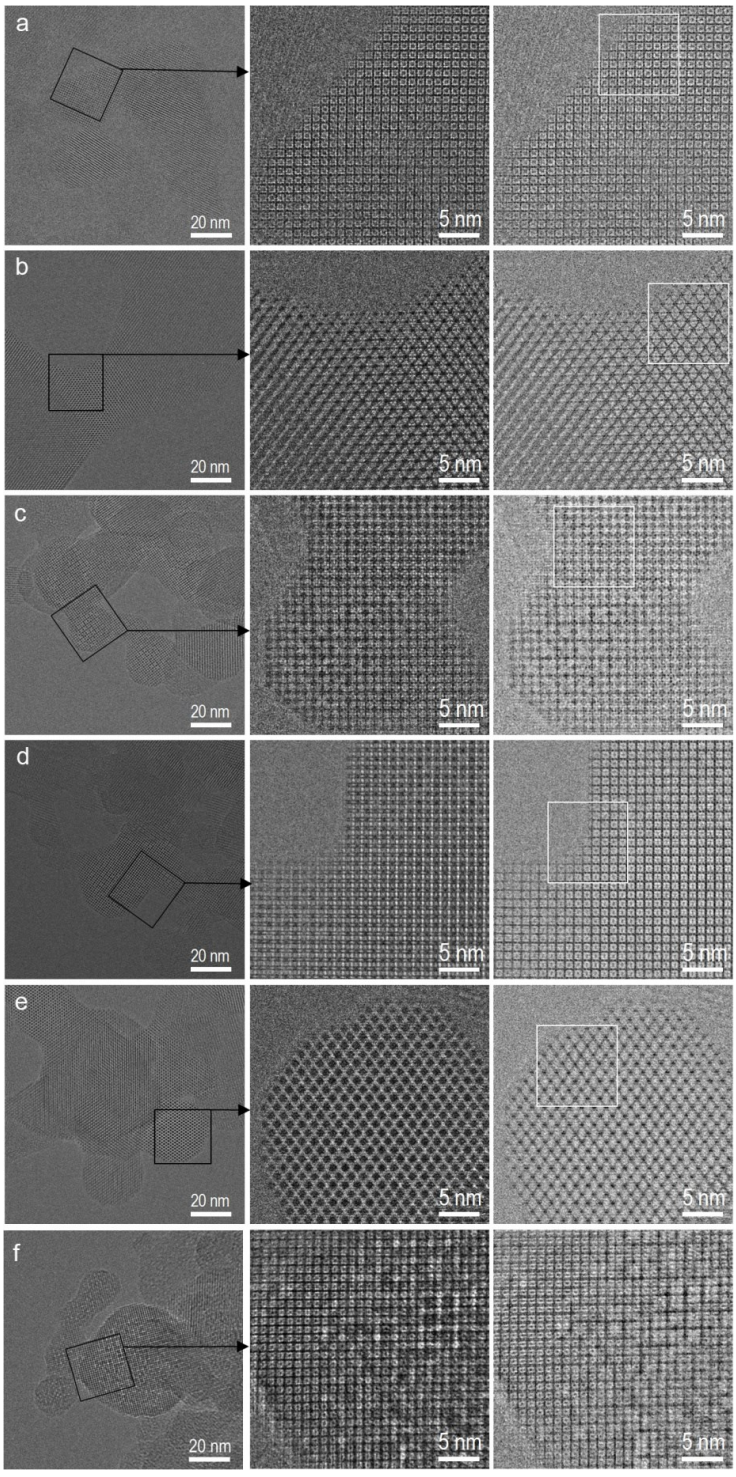

Supplementary Figure 1. Raw HRTEM images acquired from different UiO-66-D crystals and their processing: (left) raw images; (middle) the zoom-in of the regions labelled by black squares; and (right) the

corresponding CTF-corrected images. Figure 2 a-e in the main text correspond to the areas marked by white squares in **(a) - (e)**, respectively. Figure 3a and 3b in the main text are cropped images from **(c)** and **(f)**, respectively.

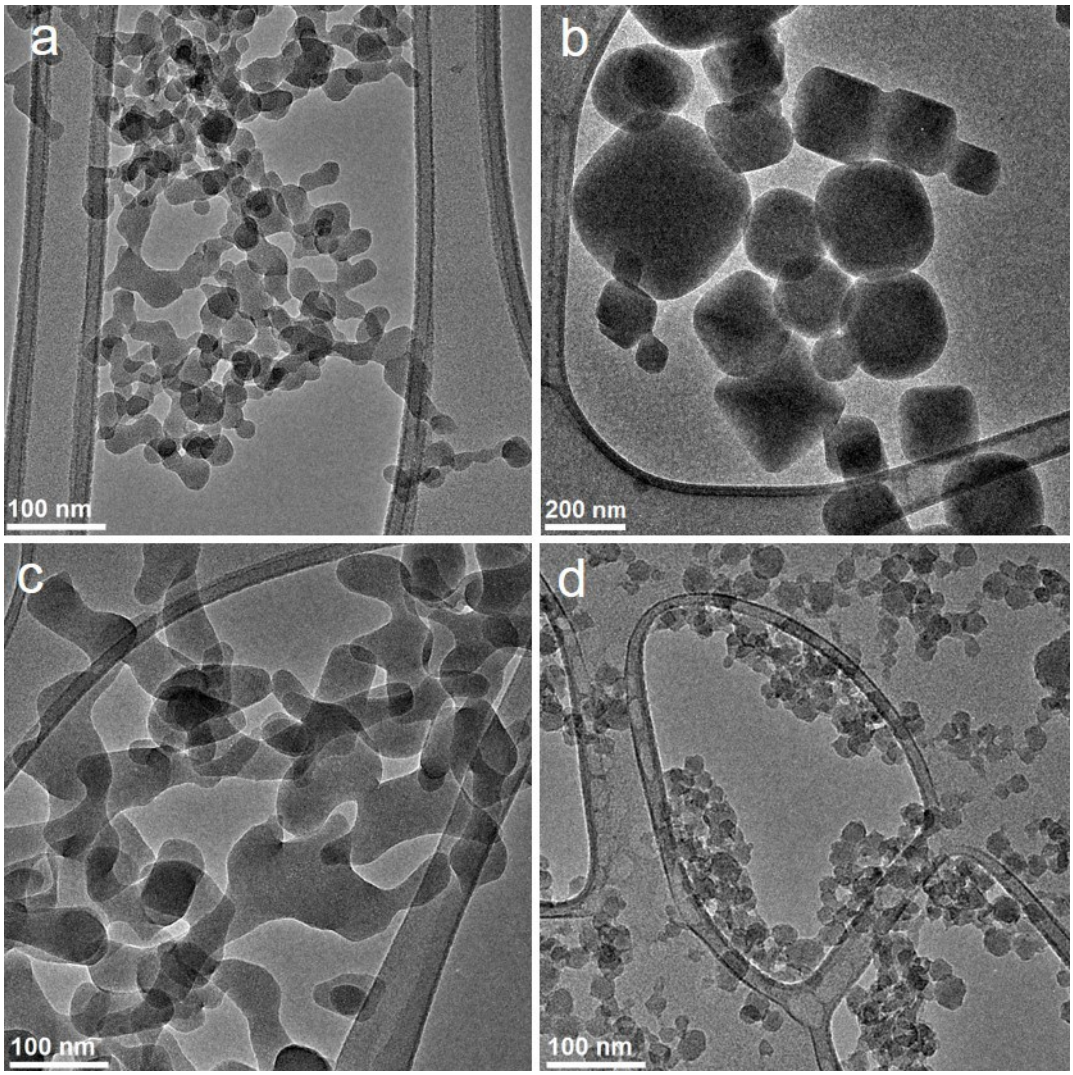

Supplementary Figure 2. Low-magnification TEM images of different UiO-66 samples: (**a**) UiO-66-D, (**b**) UiO-66-P, (**c**) UiO-66-D with prolonged crystallization time (3 days), and (**d**) UiO-66-D with shortened crystallization time (1 h). The standard UiO-66-D sample shown in (**a**) is of 1 day crystallization.

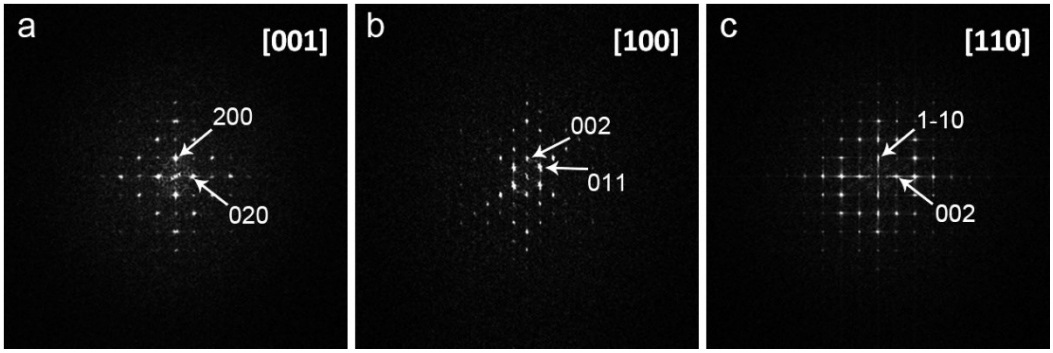

Supplementary Figure 3. (**a-c**) Fourier transform patterns of the HRTEM images shown in Figs. 2c-e, respectively. The reflections are indexed according to the tetragonal unit cell of the missing linker structure. Observed reflection conditions, *h*00: *h*=2n, 00*l*: *l*=2n, *hh*0: none, *hk*0: *h*+*k*=2n, 0*kl*: *k*+*l*=2n, *hhl*: *l* = 2n and *hkl*: *h*+*k*+*l*=2n, coincide with *I*--- space groups.

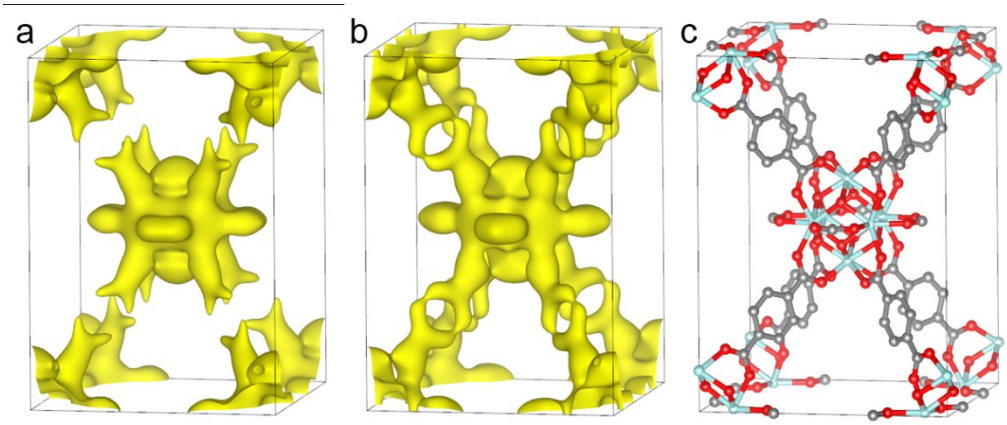

Supplementary Figure 4. Electron potential maps calculated by using different space group symmetry: **(a)** *I*422 and **(b)** *I*4/*mmm*. The amplitudes and phases of structure factors for the calculation are extracted through Fourier transform from the HRTEM shown in Figs. 2c-e. Isosurfaces shown in **(a)** and **(b)** are rendered with threshold values of 58.3% and 48.5%, respectively, relative to the maximum density. **(c)** The optimized structure model of the missing linker defect.

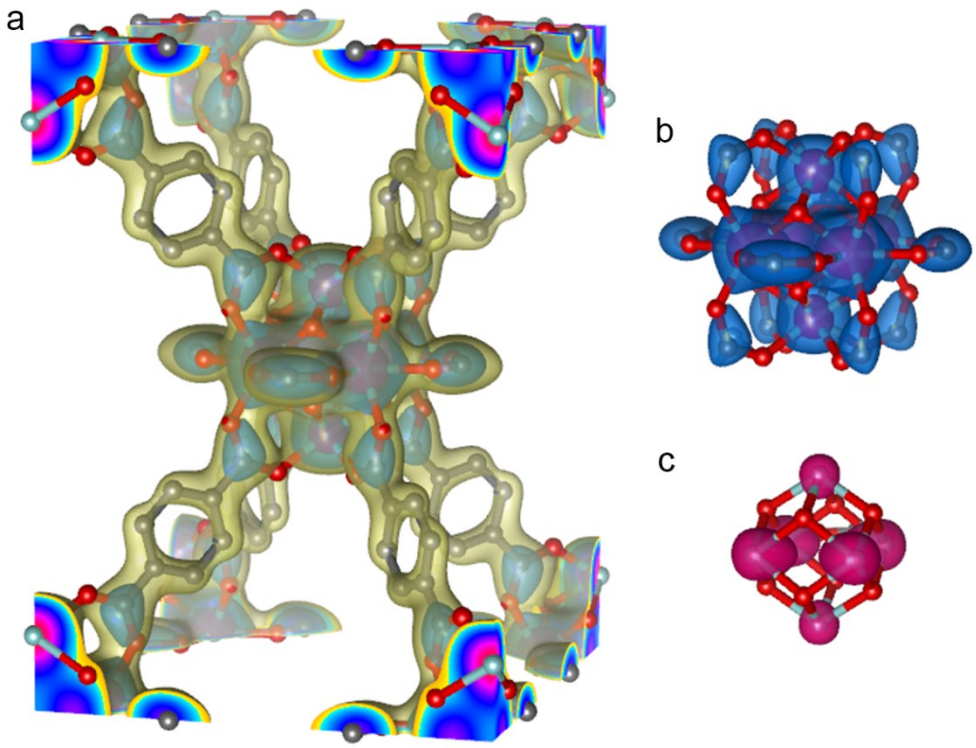

Supplementary Figure 5. Detailed analysis of the calculated electron potential map, showing the high precision of the reconstruction. Isosurfaces rendered at different thresholds are superimposed with the geometry-optimized structure model of the missing linker defect for comparison. Clearly, the envelope of the defective UiO-66 framework, which is composed of Zr cluster, BDC linkers and defect-terminating formate groups, is identified at the threshold of 48.5% **(a)**. The C atoms on carboxyl groups and the Zr atoms are precisely identified at the threshold of 56.0% (**b**) and 74.5% (**c**), respectively.

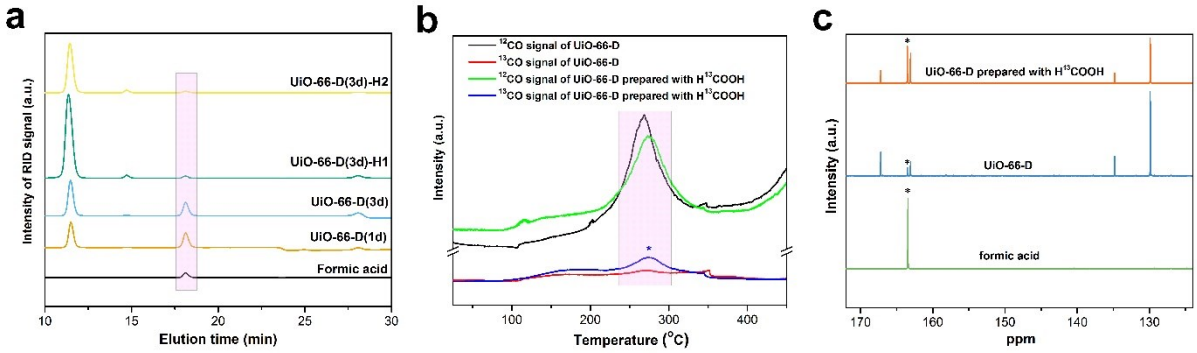

Supplementary Figure 6. (a) HPLC analysis of the HF-digested UiO-66 samples, showing the presence of formates in these materials (formic acids were detected in the digested solution). (b) Thermal gravimetric mass spectrometry (TG-MS) analysis of two UiO-66-D samples that are synthesized with conventional formic acid and ^{13}C-labelled formic acid, respectively; the results demonstrate that during the thermal decomposition process, a portion of the released CO is from formates. (c) ^{13}C NMR spectra of formic acid, UiO-66-D, and UiO-66-D prepared with ^{13}C-labelled formic acid in d6-DMSO as solvent. The asterisks (*) indicate the peak associated with formic acid.

Note: For TG-MS analysis, 50 mg of UiO-66 sample was loaded into a quartz tube placed in a fixed-bed reactor. Helium was used as carrier gas with a flow rate of 5 mL/min. The reator was purged by the helium flow for 30 min at room temperature and then heated up to 450 °C with a rate of 2 °C/min. During the heating, the outlet gases with different molecular weights were monitored by MS (OMNI^{star}). The figure above shows only MS singals of ^{12}CO and ^{13}CO.

For ^{13}C NMR analysis, 50 mg of UiO-66 sample was digested by a mixture solution of 47 wt% HF (40 µL) and 0.5 mL of *d*6-DMSO. After centrifugation, the upper clear solution was transferred into a NMR tube, and analyzed on a Bruker 600 MHz spectrometer (Ultrashield 600 PLUS).

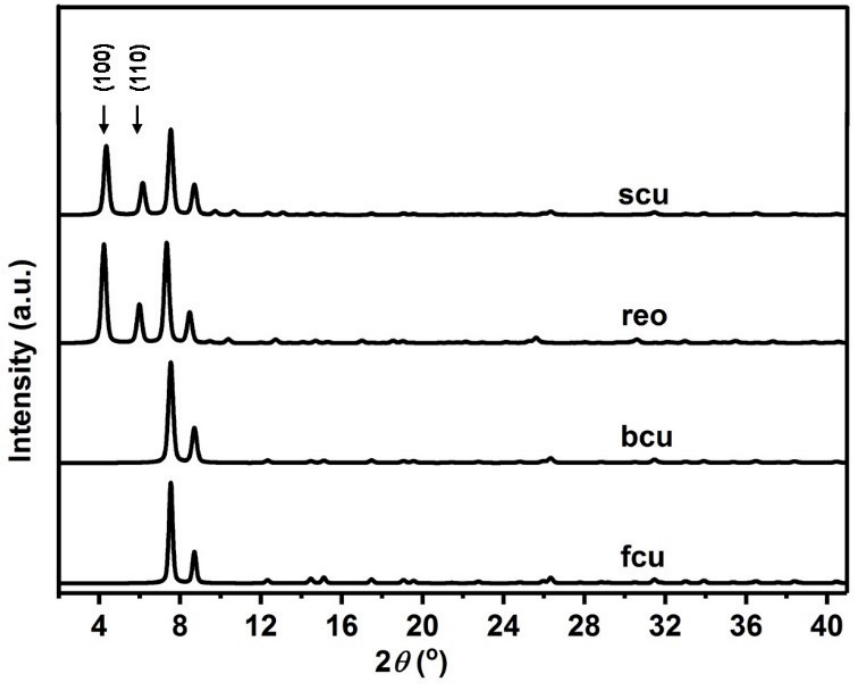

Supplementary Figure 7. Simulated PXRD patterns are based on different structure models, perfect UiO-66 model with **fcu** topology, the missing linker model with **bcu** topology, the missing cluster model with **reo** topology, and the missing cluster model with **scu** topology.

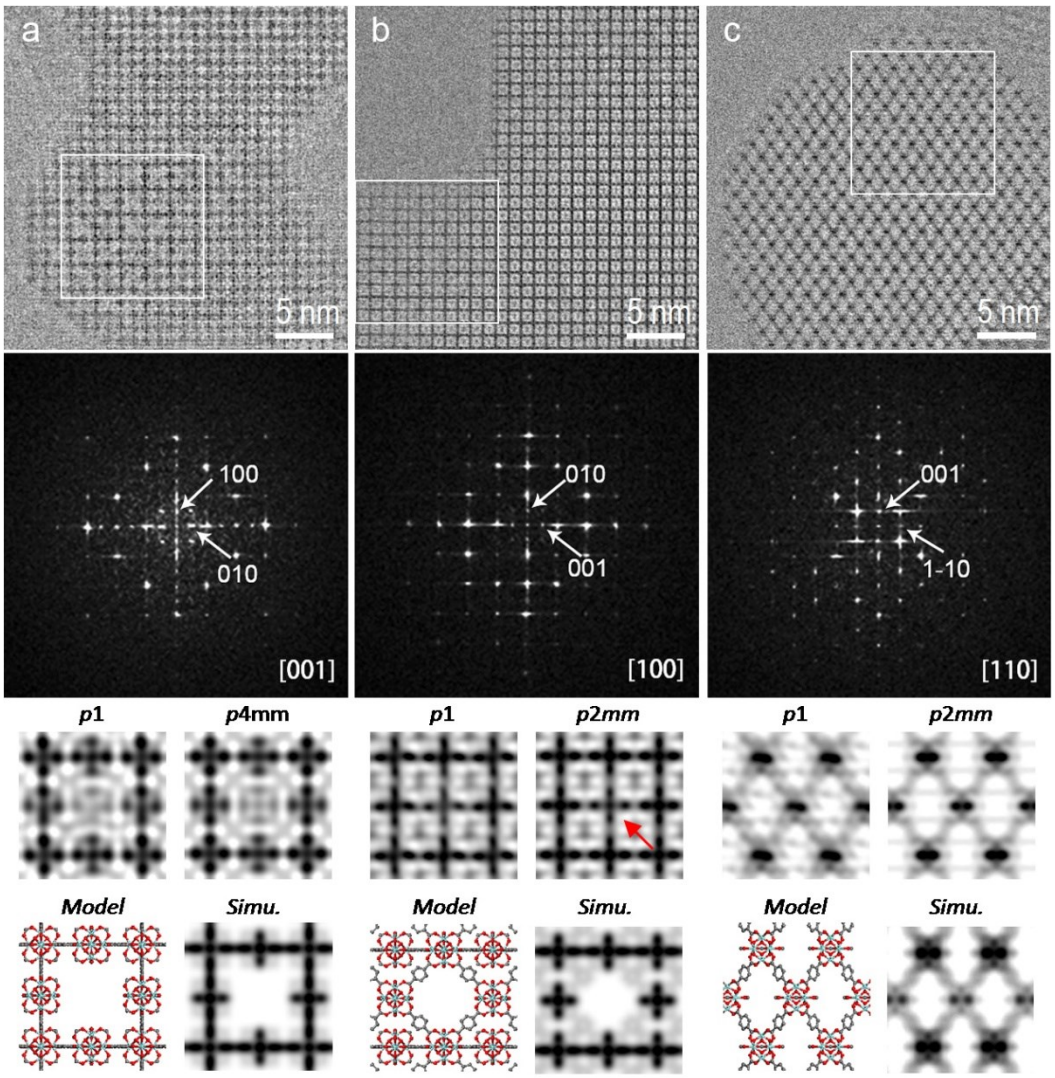

Supplementary Figure 8. a-c, Analysis of the missing cluster defects along different directions: (**a**) [001], (**b**) [100], and (**c**) [110]. (Top) CTF-corrected HRTEM images; (middle) Fourier transform patterns from the areas labelled in the HRTEM images with white squares; (bottom) Results of projection symmetry analysis, projected structural models, and simulated potential maps. The *p*1-averaged and symmetry imposed maps are calculated using crystallographic software CRISP. The projection symmetries of the images, *p*4*mm* for (**a**), *p*2*mm* for (**b**) and *p*2*mm* for (**c**), are determined as the highest symmetry with reasonable Phase residuals (ϕRes< 15%). Superlattice reflections that correspond to the extinct 100 and 110 reflections of pristine UiO-66 are observed in all directions, due to the presence of missing cluster defects. The structural models and simulated potential maps are based on the **scu** missing cluster model, which can be directly deduced from the [001] image (see Supplementary fig. 9). Experimental and simulated projected potentials match well in all directions, except that the experimental image of the [100] direction (**b**) shows residual contrast for the missing cluster, as pointed by the red arrow. It

is reasonable to attribute the observed residual contrast to the overlapping of missing linker and missing cluster domains in the projection direction, given that the missing cluster domains are very small. In the other two directions, the characteristic image contrasts of the **scu** structure, the missing of linkers around the missing cluster in the [001] direction and the complete absence of horizontal BDC linkers in the [110] direction (see Supplementary Fig. 10), are clearly observed.

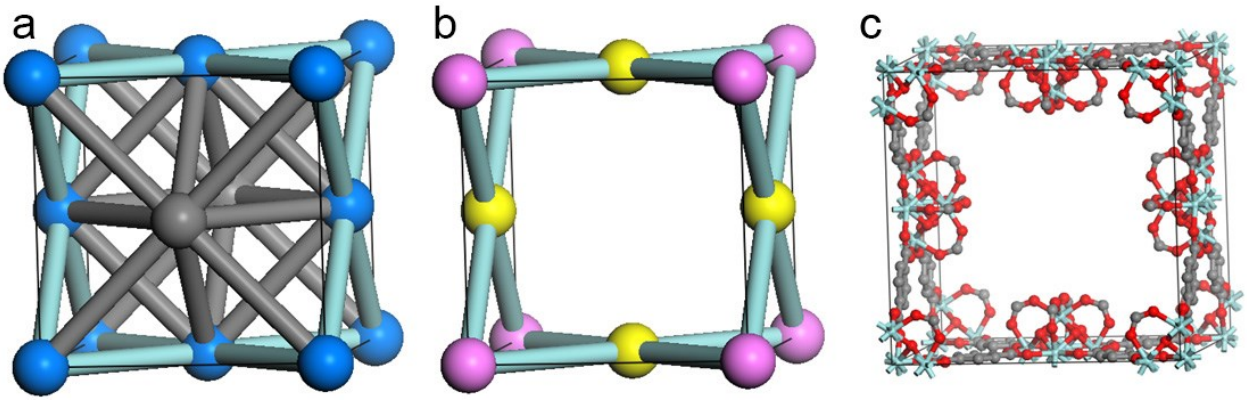

Supplementary Figure 9. Derivation of the **scu** missing cluster model from the ideal UiO-66 structure. **(a)** The 12-connected **fcu** net of ideal UiO-66, in which the missing components (both nodes and linkers), as determined based on image contrast (see Fig. 3b in the main text), are marked in gray. The removal of these components from **(a)** leads to **(b)**, the 4- and 8-connected **scu** net. **(c)** The corresponding crystal structure model of **(b)**. Blue (or grey), pink and yellow balls in **(a)** and **(b)** indicate 12-, 8- and 4-connected nodes, respectively. The as-derived missing cluster model (space group: *P*4/*mmm*) provides a unique solution of the structure, because the operation of further removing any linkers from this model would break the 3D continuous framework, given the symmetry observed in Supplementary Fig. 8. Moreover, the simulated projected potential maps based on this model match the experimental HRTEM images in all directions, as shown in Supplementary Fig. 8, which further testifies that the model is correct.

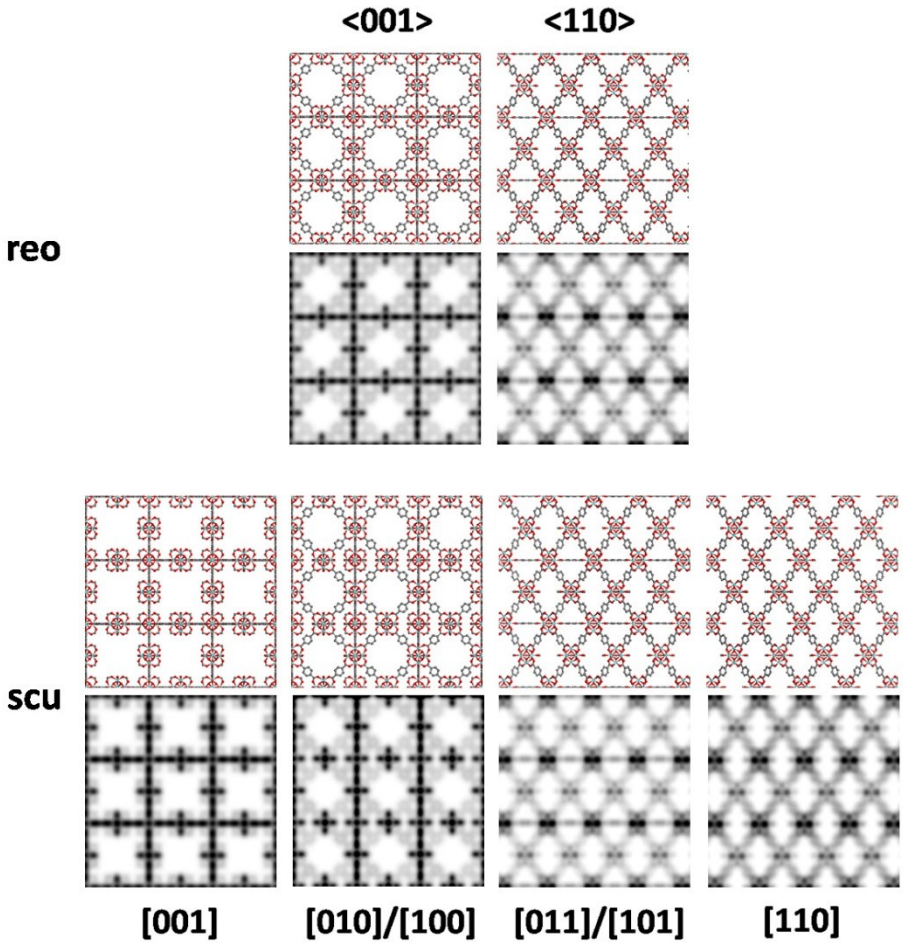

Supplementary Figure 10. Projected structural models and simulated potential maps of two types of missing cluster defects: the cubic **reo** and the tetragonal **scu**, along different crystallographic directions. The <001> of **reo** is similar to the [010]/[[100] of **scu** (slight difference in plane symmetry: *p*4*mm* versus *p*2*mm*), and the <110> of **reo** is similar to the [011]/[[101] of **scu**. Therefore, it is difficult to distinguish the two models in these directions. On the contrary, the [001] and [110] projections of **scu** are characteristic, which show *the missing of linkers around the missing cluster* and *the complete absence of horizontal BDC linkers*, respectively.

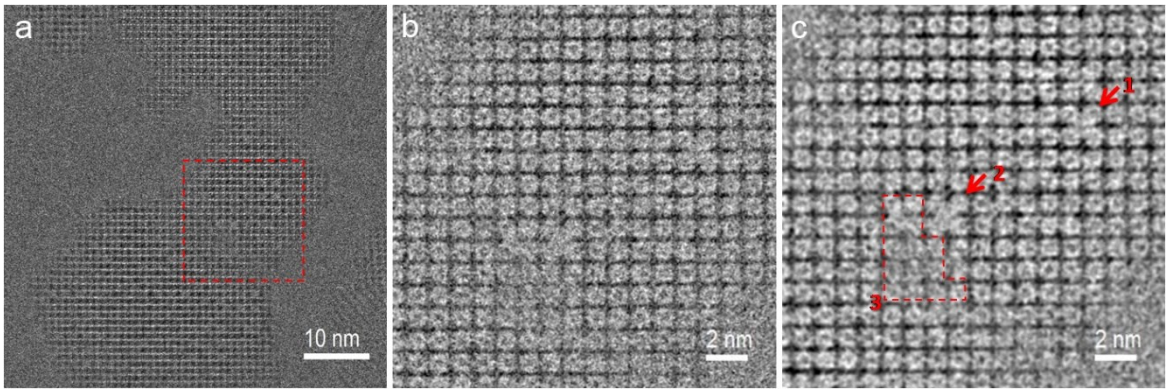

Supplementary Figure 11. (**a**) Raw, (**b**) CTF-corrected, and (**c**) filtered CTF-corrected HRTEM images of a UiO-66-D crystal, showing the diversity of missing cluster defects in this material. (**b**) and (**c**) are cropped from the marked region in (**a**). In (**c**), the lattice cells labeled with **1** and **2** correspond to the **reo** and **scu** missing cluster defect, respectively. The area labeled with **3** represents a large cavity resulting from irregular, continuous cluster vacancies.

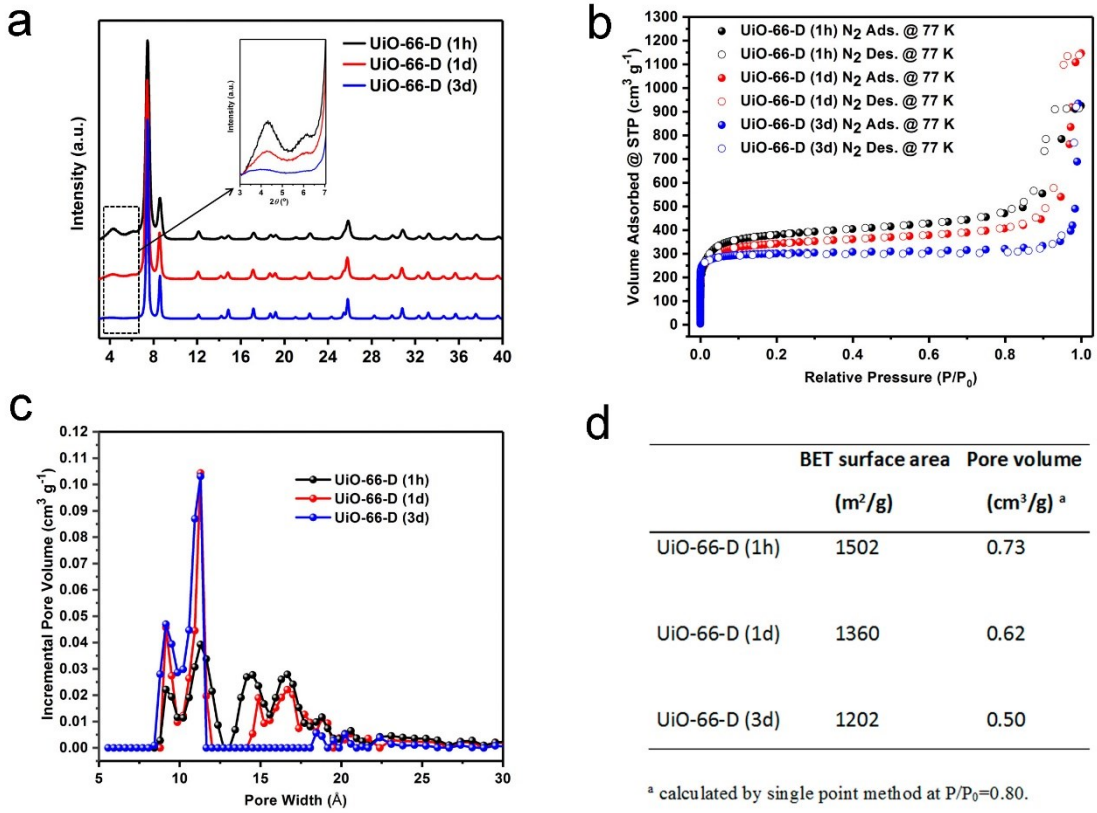

d

	BET surface area (m^2/g)	Pore volume (cm^3/g) [a]
UiO-66-D (1h)	1502	0.73
UiO-66-D (1d)	1360	0.62
UiO-66-D (3d)	1202	0.50

[a] calculated by single point method at P/P_0=0.80.

Supplementary Figure 12. (**a**) PXRD, (**b**) N_2 sorption isotherm and (**c**) pore size distribution profiles of the UiO-66-D samples synthesized with different crystallization time, 1 hour (1h), 1 day (1d) and 3 days (3d). Inset of (**a**) highlights the diffuse scattering peaks at the low angle region. (**d**) BET surface areas and pore volumes of the three samples derived from the isotherms. The PXRD and N_2 sorption data are in agreement, showing that missing cluster defects gradually vanish with prolonged crystallization.

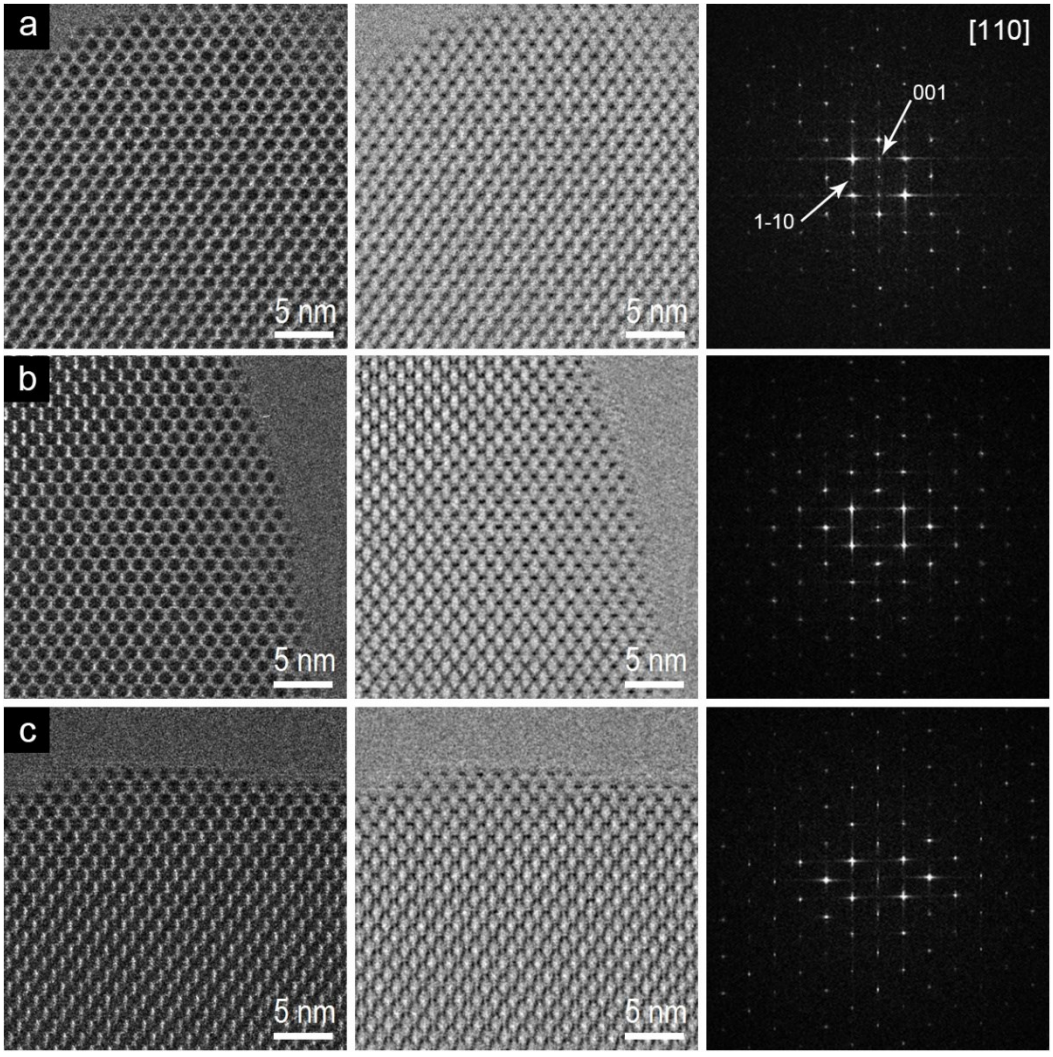

Supplementary Figure 13. HRTEM of UiO-66 samples synthesized from different conditions: (**a**) UiO-66-D crystallized for 1 hour, (b) UiO-66-D crystallized for 3 days, and (c) UiO-66-P synthesized by using acetic acid as modulator. (Left) raw HRTEM images; (middle) CTF-corrected images; (right) the corresponding FT patterns. These images are along the [110] direction, all showing the "missing linker" feature (i.e., no contrast of the BDC ligand observed in the rhombus-shaped channels). Superlattice reflections are observed in the FT pattern in (**a**), indicating the presence of missing cluster defects in the 1h sample. Superlattice reflections are hardly observed in the other two samples.

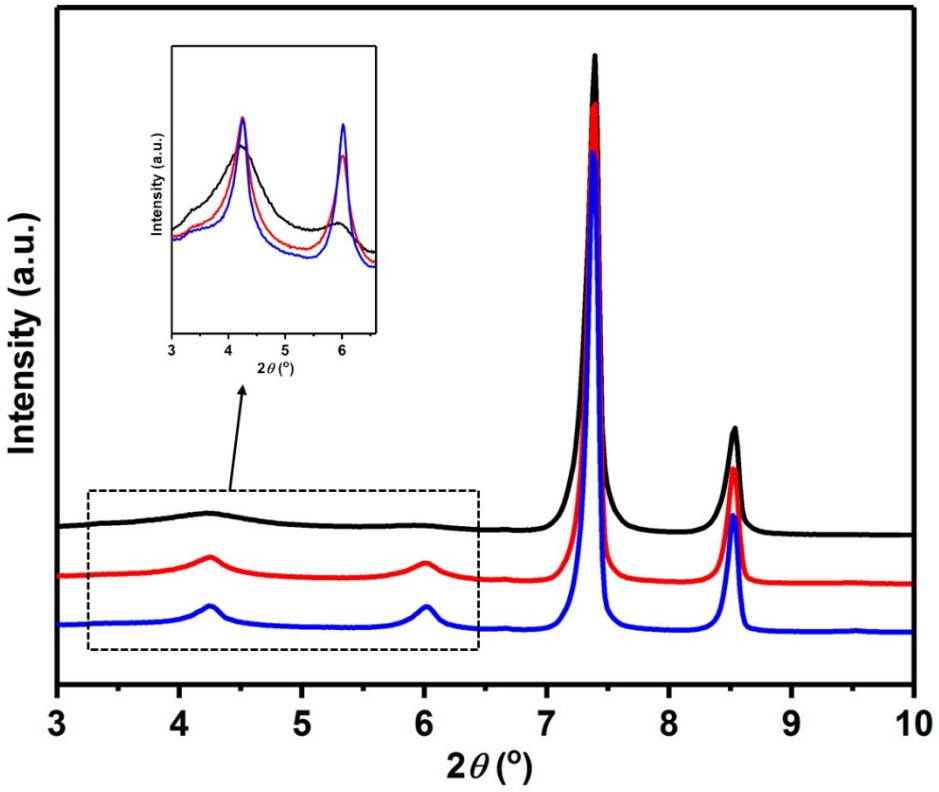

Supplementary Figure 14. PXRD patterns of UiO-66 synthesized using 175 molar equivalents of formic acid relative to BDC at different crystallization time (Black: 1 hour; Red: 1 day; Blue: 2days). The inset highlights the diffuse scattering peaks at low angle region. The results show that missing cluster defects are rapidly developed and grown as the crystallization time increases, namely, a reverse trend of defect evolution compared to the system using 50 molar equivalents of formic acid (Supplementary Fig. 12).

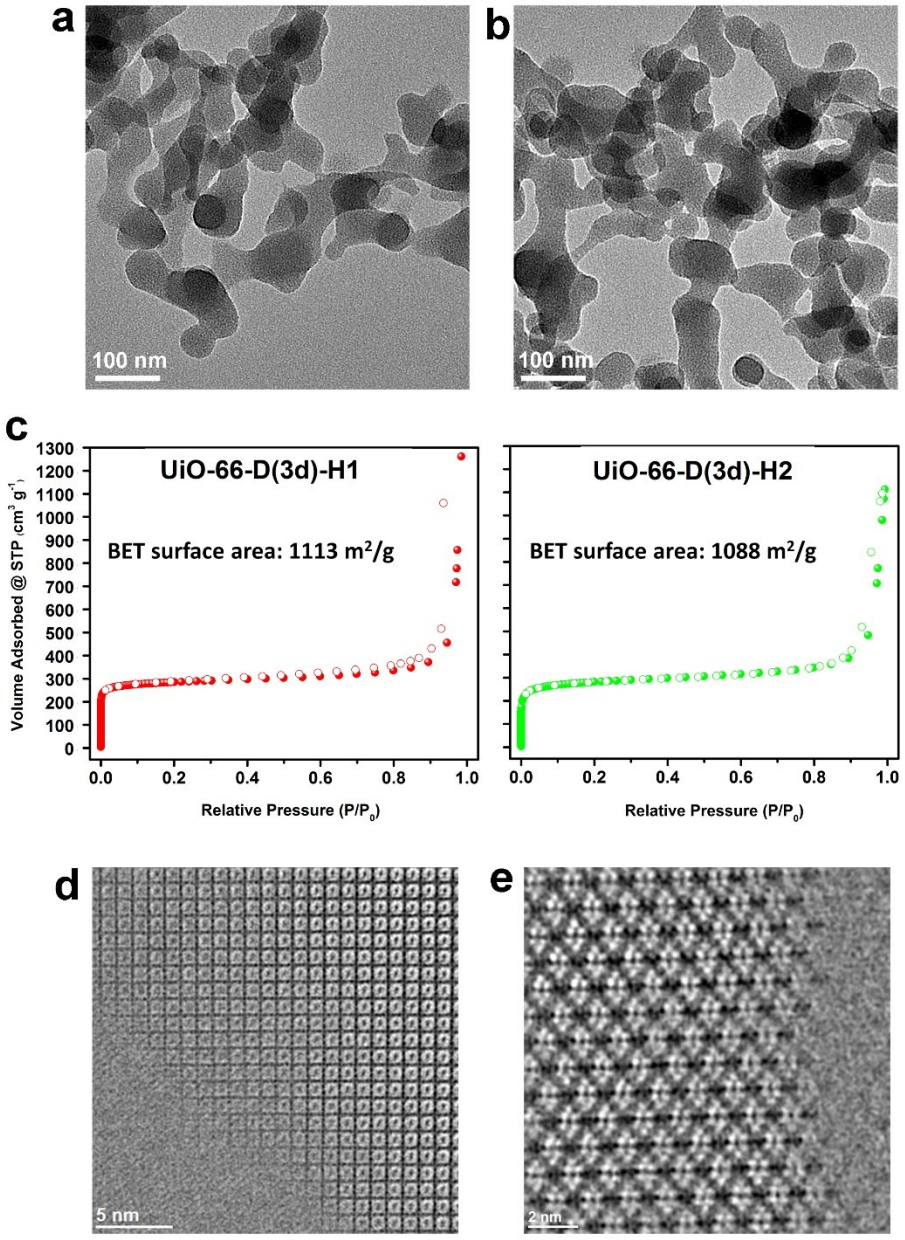

Supplementary Figure 15. (a-b) Low-mag TEM images of UiO-66-D(3d)-H1 (a) and UiO-66-D(3d)-H2 (b). (c) N_2 sorption isotherms of UiO-66-D(3d)-H1 and UiO-66-D(3d)-H2 collected at 77K. (d-e) HRTEM images of UiO-66-D(3d)-H2 acquired along the [001] (d) and the [110] (e) incidence, showing the "perfect" UiO-66 structure. Note that using HRTEM, we observed the "perfect" structure much more frequently in the healed samples (UiO-66-D(3d)-H1 or UiO-66-D(3d)-H2) than in UiO-66-D(3d).

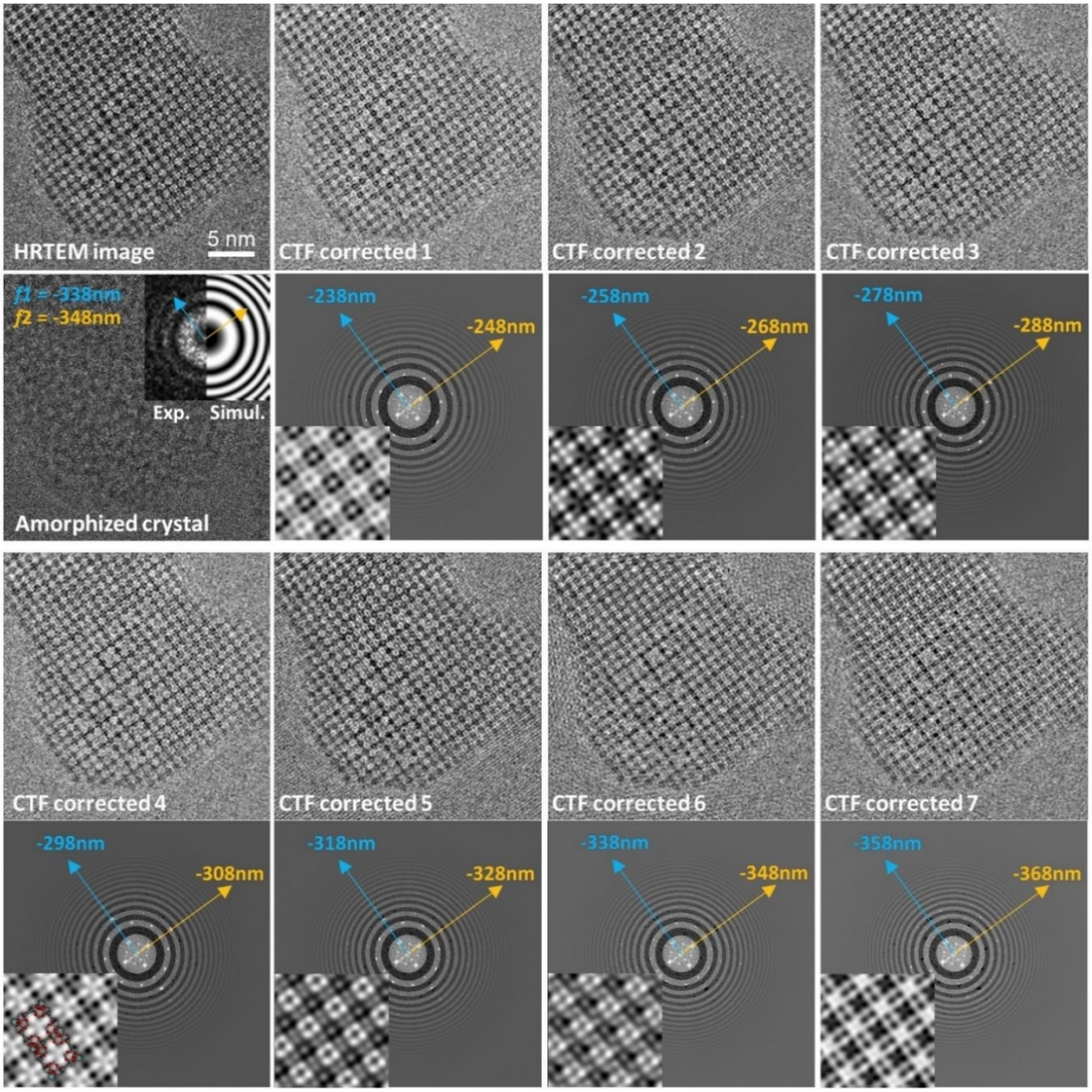

Supplementary Figure 16. Illustration of the defocus determination. After acquiring an HRTEM image (row 1, the first from the left), the crystal is purposely amorphized by the electron beam (row 2, the first from the left). Then, CTF correction is applied using a range of defocus values around the defocus determined from the amorphous specimen, and the corrected images are shown in the rest 7 panels. For each condition, phase flipped zones are shown as negative values (black contrast) in the FT pattern, and the lattice averaged image is shown as insets. The defocus values are finally determined to be the values shown in "CTF corrected 4" because the corresponding processed image gives the most reasonable contrast to show five Zr atom columns, in agreement with the [001] projection of UiO-66. Due to the space limitation, 20 nm step size is used here to illustrate the method; in real cases, 1 nm step size is used to avoid missing the right conditions. The CTF-corrected images shown here have been denoised by using a Gaussian blur filter with $\sigma = 2$ pixels.

Supplementary Table 1: Formation energies ΔE (in kJ/mol per 3×Zr) of different types of defects in UiO-66(Zr).

Defect type	ΔE
bcu	17.8
reo	20.4
scu	32.4

The defect formation energies were calculated according to the following reactions:

$$\Delta E_{fcu\rightarrow bcu} = \frac{1}{8}E_{bcu} - \frac{1}{8}E_{fcu} + E_{H2BDC} - 2 \times E_{formic\ acid}$$

$$\Delta E_{fcu\rightarrow reo} = \frac{1}{6}E_{reo} - \frac{1}{8}E_{fcu} + E_{H2BDC} - 2 \times E_{formic\ acid}$$

$$\Delta E_{fcu\rightarrow scu} = \frac{1}{6}E_{scu} - \frac{1}{8}E_{fcu} + \frac{5}{3}E_{H2BDC} - \frac{10}{3}E_{formic\ acid}$$

in which the energies of H_2BDC and formic acid were calculated from isolated gas phase molecules. Following the experimental synthesis recipe, we only consider formate as the charge-compensating species. We note the nature and concentration of defects observed in experiment are sensitive to the charge compensation mechanism and the concentration and acidity of the modulator used [19].

We note that there is discrepancy between the absolute concentration of defects observed experimentally and the populations derived from the calculated absolute defect formation energies. For example, the calculated defect formation energy of **bcu** is 17.8 kJ/mol, corresponding to a concentration of 0.08% (assuming room temperature), which is approximately 13-fold lower than the lowest "missing linker" concentration (~1%) determined based on the formate content. This discrepancy is understandable considering that the defect concentration has an exponential dependence on the formation energy, and a small change in defect formation energy will yield a significant change to the predicted concentration of defects. We also note that predicting absolute thermochemical reaction energies within the approximations present in density functional theory to within even a 10-20 kJ/mol absolute error with respect to experiment is extremely challenging. Moreover, we use total energy differences computed at 0 K rather than free energies at a finite temperature, since vibrational free energy calculations are prohibitively computationally expensive. Presumably, the more undercoordinated defective lattices have higher vibrational entropy, so it is likely that the defect formation energy we report is slightly overestimated with respect to the true free energy difference. We also neglect solvent, as the intrinsic random errors associated with modelling solvent could be comparable with the energy range we examine. It is conceivable that solvent is more structured around the formate ligands, which would stabilise the

defective structures and reduce the defect formation energy. Putting these considerations together, the discrepancy between the observed concentration and the computed concentration of defects is minor.

Supplementary Table 2: Computationally predicted helium-accessible pore volume (in cm^3g^{-1}) and N_2-accessible surface area (in m^2g^{-1}) of the perfect and defective UiO-66 structures.

Structure	Accessible pore volume / cm^3g^{-1}	Accessible surface area / m^2g^{-1}
fcu	0.42	1158
bcu	0.52	1813
reo	0.82	2208
scu	0.91	2559

Note: The predicted surface area of fcu happens to be almost identical to the experimentally measured value of 1159 m^2g^{-1} for UiO-66-P and both the computed and measured values are within the bounds recently identified in a comprehensive study by Park, Howe and Sholl [43]. However, we note the simulated surface area is likely to be an overestimate as the experimental sample used contains a non-negligible number of defects and has an external surface whereas the modelled material contains no defects and is a boundary free material.

The helium-accessible pore volume and N_2-accessible surface area of the perfect and defective UiO-66 structures were calculated using the RASPA software package [Suppl. Ref. 13, 14]. Cell parameters and positions of framework atoms were taken from our DFT optimized structures. The adsorbate-adsorbate and adsorbate-framework interactions are calculated with a pairwise Lennard-Jones potential, where the adsorbate atom ϵ and σ parameters are taken from the TraPPE force field [https://github.com/numat/RASPA2/tree/master/forcefield/TraPPE. Accessed 8 January 2019.], and the framework atom ϵ and σ parameters are taken from the GenericMOFs force field [https://github.com/numat/RASPA2/tree/master/forcefield/GenericMOFs. Accessed 8 January 2019.] within the RASPA software package. Individual pairwise interaction parameters are obtained by Lorentz–Berthelot mixing rules.

Supplementary Table 3: Experimental structure factors from of linker missing UiO-66.

[001] Zone axis

h	*k*	*l*	Amp.	Pha.
1	-1	0	10000	0
2	-2	0	1720	0
3	-3	0	8939	0
4	-4	0	1077	0
5	-5	0	1008	0
2	0	0	1355	π
3	-1	0	5390	π
4	-2	0	1178	0
5	-3	0	809	0
6	-4	0	620	π
4	0	0	604	π
5	-1	0	792	π
7	-3	0	638	π
6	0	0	1154	0
7	-1	0	611	0

[110] Zone axis

h	*k*	*l*	Amp.	Pha.
1	-1	0	9449	0
2	-2	0	8405	0
3	-3	0	4636	0
4	-4	0	1527	0
5	-5	0	837	0
0	0	2	10000	0
1	-1	2	711	0
2	-2	2	4546	π
3	-3	2	734	π
0	0	4	7965	0
1	-1	4	4329	π
2	-2	4	2861	π
0	0	6	5617	0
1	-1	6	1357	0
3	-3	6	628	0
0	0	8	833	0
3	-3	8	451	0
0	0	10	932	0

[010] Zone axis

h	*k*	*l*	Amp.	Pha.
2	0	0	536	π
4	0	0	635	π
6	0	0	437	0
1	0	1	10000	0
3	0	1	636	0
5	0	1	812	π
7	0	1	543	0
0	0	2	3967	0
2	0	2	4701	0
4	0	2	1167	π
6	0	2	401	π
1	0	3	2199	0
3	0	3	1319	0
5	0	3	918	π
0	0	4	690	π
2	0	4	1041	π
4	0	4	1270	π
6	0	4	457	π
1	0	5	1993	0
3	0	5	883	0
5	0	5	739	π
0	0	6	3992	0
2	0	6	425	0
4	0	6	879	0
6	0	6	587	π
1	0	7	1053	0
0	0	8	1325	0
2	0	8	619	0
4	0	8	496	Π
1	0	9	432	0

Supplementary Table 4: Merged experimental structure factors for linker missing UiO-66.

Merged structure factors from three zone axes

h	*k*	*l*	Amp.	Pha.	*h*	*k*	*l*	Amp.	Pha.
2	0	0	1069	π	0	0	8	846	0
4	0	0	510	π	2	0	8	619	0
6	0	0	707	0	4	0	8	496	π
1	0	1	10000	0	1	0	9	432	0
3	0	1	636	0	1	-1	0	4666	0
5	0	1	812	π	2	-2	0	2297	0
7	0	1	543	0	3	-3	0	4617	0
0	0	2	4188	0	4	-4	0	615	0
2	0	2	4701	0	5	-5	0	445	0
4	0	2	1167	π	3	-1	0	2784	π
6	0	2	401	π	4	-2	0	608	0
1	0	3	2199	0	5	-3	0	418	0
3	0	3	1319	0	6	-4	0	320	π
5	0	3	918	π	5	-1	0	409	π
0	0	4	2101	π	7	-3	0	330	π
2	0	4	1041	π	7	-1	0	316	0
4	0	4	1270	π	1	-1	2	290	0
6	0	4	457	π	2	-2	2	1857	π
1	0	5	1993	0	3	-3	2	300	π
3	0	5	883	0	1	-1	4	1768	π
5	0	5	739	π	2	-2	4	1169	π
0	0	6	3234	0	1	-1	6	554	0
2	0	6	425	0	3	-3	6	257	0
4	0	6	879	0	3	-3	8	184	0
6	0	6	587	π	0	0	10	381	0
1	0	7	1053	0					

Supplementary Table 5: Cell parameters and space groups of different phases

Topology	Methods	*a* (Å)	*b* (Å)	*c* (Å)	Crystal system	Space group (DFT*)	Space group (Experimental)
fcu	DFT	20.917	20.917	20.917	Cubic	*F*-43*m*	*Fm*-3*m*
bcu	DFT	14.764	14.764	20.923	Tetragonal	*I*-4*m*2	*I*4/*mmm*
reo	DFT	20.908	20.908	20.908	Cubic	*P*-43*m*	*P*-43*m* ^
scu	DFT	20.882	20.882	20.913	Tetragonal	*P*-42*m*	*P*4/*mmm*

** Optimized space group symmetries of DFT structure models are determined with a tolerance limit of 0.05Å. The difference in space group between the last two columns is because hydrogens are invisible in the experimental results. ^ The space group of reo structure was from reference [25]; the limited experimental data about reo in this work is insufficient for space group determination.*

Supplementary References:

1. QSTEM V2.31 (http://www.qstem.org)
2. Hovmoller, S., CRISP: crystallographic image processing on a personal computer. *Ultramicroscopy* **41,** 121-135 (1992).
3. Momma, K. and Izumi, F., VESTA 3 for three-dimensional visualization of crystal, volumetric and morphology data. *J. Appl. Crystallogr.*, **44,** 1272-1276 (2011).
4. VandeVondele, J., Krack, M., Mohamed, F., Parrinello, M., Chassaing, Thomas, Hutter, J., QUICKSTEP: Fast and accurate density functional calculations using a mixed Gaussian and plane waves approach. *Comput. Phys. Commun.*, **167,** 103-128 (2005).
5. VandeVondele, J. and Hutter, J., Gaussian basis sets for accurate calculations on molecular systems in gas and condensed phases. *J. Chem. Phys.,* **127,** 114105-114109 (2007).
6. Hutter, J., Iannuzzi, M., Schiffmann, F., VandeVondele, J., cp2k: atomistic simulations of condensed matter systems. *Comput. Mol. Sci*., **4,** 15–25 (2014).
7. Goedecker S., Teter M., and Hutter. J., Separable dual-space Gaussian pseudopotentials. *Phys. Rev. B*, **54,** 1703-1710 (1996).
8. Krack M., Pseudopotentials for H to Kr optimized for gradient-corrected exchange-correlation functionals. *Theor Chem Acc*, **114,** 145–152 (2005).
9. Perdew, J. P., Burke, K., and Ernzerhof, M., Generalized Gradient Approximation Made Simple. *Phys. Rev. Lett.*, **77,** 3865-3868 (1996).
10. Grimme S., Antony J., Ehrlich S., Krieg H., A consistent and accurate ab initio parametrization of density functional dispersion correction (DFT-D) for the 94 elements H-Pu. *J. Chem. Phys.,* **132,** 154104-154119 (2010).
11. Ling S. and Slater B., Dynamic acidity in defective UiO-66. *Chem. Sci.*, **7,** 4706-4712 (2016).
12. Nanthamathee C., Ling S., Slater B., Attfield M. P., Contradistinct thermoresponsive behavior of isostructural MIL-53 type metal–organic frameworks by modifying the framework inorganic anion. *Chem. Mater.*, **27,** 85–95 (2015).
13. Dubbeldam, D., Calero, S., Ellis, D. E. & Snurr, R.Q. RASPA: molecular simulation software for adsorption and diffusion in flexible nanoporous materials, *Mol. Simul*. **42,** 81-101 (2016).
14. Dubbeldam, D., Torres-Knoop, A. & Walton, K. S. On the inner workings of Monte Carlo codes, *Mol. Simul*. **39,** 1253-1292 (2013).